Technical Note: Characterization and correction of gradient nonlinearity induced distortion on a 1.0 T open bore MR-SIM

Ryan G. Price
Department of Radiation Oncology, Henry Ford Health System, Detroit, Michigan 48202 and Department of Radiation Oncology, Wayne State University School of Medicine, Detroit, Michigan 48201

Mo Kadbi
Philips Healthcare, Cleveland, Ohio 44143

Joshua Kim
Department of Radiation Oncology, Henry Ford Health System, Detroit, Michigan 48202

James Balter
Department of Radiation Oncology, University of Michigan, Ann Arbor, Michigan 48109

Indrin J. Chetty and Carri K. Glide-Hurst[a)]
Department of Radiation Oncology, Henry Ford Health System, Detroit, Michigan 48202 and Department of Radiation Oncology, Wayne State University School of Medicine, Detroit, Michigan 48201

(Received 5 February 2015; revised 11 August 2015; accepted for publication 21 August 2015; published 22 September 2015)

Purpose: Distortions in magnetic resonance imaging (MRI) compromise spatial fidelity, potentially impacting delineation and dose calculation. We characterized 2D and 3D large field of view (FOV), sequence-independent distortion at various positions in a 1.0 T high-field open MR simulator (MR-SIM) to implement correction maps for MRI treatment planning.
Methods: A $36\times43\times2$ cm^3 phantom with 255 known landmarks (~1 mm^3) was scanned using 1.0 T high-field open MR-SIM at isocenter in the transverse, sagittal, and coronal axes, and a $465\times350\times168$ mm^3 3D phantom was scanned by stepping in the superior-inferior direction in three overlapping positions to achieve a total $465\times350\times400$ mm^3 sampled FOV yielding >13 800 landmarks (3D Gradient-Echo, TE/TR/α = 5.54 ms/30 ms/28°, voxel size = $1\times1\times2$ mm^3). A binary template (reference) was generated from a phantom schematic. An automated program converted MR images to binary via masking, thresholding, and testing for connectivity to identify landmarks. Distortion maps were generated by centroid mapping. Images were corrected via warping with inverse distortion maps, and temporal stability was assessed.
Results: Over the sampled FOV, non-negligible residual gradient distortions existed as close as 9.5 cm from isocenter, with a maximum distortion of 7.4 mm as close as 23 cm from isocenter. Over six months, average gradient distortions were -0.07 ± 1.10 mm and 0.10 ± 1.10 mm in the x and y directions for the transverse plane, 0.03 ± 0.64 and -0.09 ± 0.70 mm in the sagittal plane, and 0.4 ± 1.16 and 0.04 ± 0.40 mm in the coronal plane. After implementing 3D correction maps, distortions were reduced to <1 pixel width (1 mm) for all voxels up to 25 cm from magnet isocenter.
Conclusions: Inherent distortion due to gradient nonlinearity was found to be non-negligible even with vendor corrections applied, and further corrections are required to obtain 1 mm accuracy for large FOVs. Statistical analysis of temporal stability shows that sequence independent distortion maps are consistent within six months of characterization. [http://dx.doi.org/10.1118/1.4930245]

Key words: MRI, treatment planning, distortion, correction, gradient non-linearity

1. INTRODUCTION

Due to its superior soft tissue contrast, using magnetic resonance imaging (MRI) can result in more accurate structure delineation than computed tomography (CT).[1,2] Typically, MRI is used to define the target and organs at risk (OARs) and contours are transferred to the CT via image registration, which is then used for treatment planning and dose calculations. However, this workflow increases the clinical workload, while co-registration of MR and CT images may introduce additional systematic uncertainties that can be detrimental to target and OAR localization.[3–5] Therefore, implementing MR as a stand-alone simulation modality for radiation therapy treatment planning (RTP) is advantageous.

Implementation of MRI for single modality simulation is limited by the lack of electron density information for dose calculation, as well as both patient-induced and system-level distortions that significantly degrade treatment planning accuracy.[6,7] To support MR-only simulation, we[8] and others[9–12] have demonstrated the feasibility of generating synthetic CTs

or implementing bulk density overrides for dose calculation and DRR generation. Patient-induced distortions from susceptibility and chemical shift have shown a dependence on field strength and can be considered clinically negligible for low field systems,[13,14] such as our 1.0 T MR simulator (MR-SIM). System-level distortions arise from the inhomogeneities in the B_0 field and nonlinearities in the spatial encoding gradients. We have previously reported on our magnet's B_0 field inhomogeneity and found that it was within American College of Radiology guidelines.[15] This technical note focuses on the technical characterization of gradient nonlinearity (GNL) for large fields of view (FOVs), develops and evaluates a correction scheme, and then quantifies the temporal stability of the measurements for a clinically available MR-SIM system. GNL is the focus of this work, because it is one of the dominant sources of image distortion[16,17] and is insensitive to the acquisition sequence.[18] In this manner, clinical recommendations regarding the frequency of measurement and robustness of results for ongoing quality assurance (QA) can be ascertained to support MR-simulation for single modality RTP.

2. METHODS AND MATERIALS

2.A. Large field of view distortion phantoms

For routine temporal GNL measurements, a $36\times43\times2$ cm^3 distortion phantom (Philips Medical Systems, Cleveland, OH) consisting of 255 capsule-shaped landmarks with ~4 mm radius and 25 mm centroid-to-centroid spacing was used. The phantom can be oriented in cardinal directions (axial, sagittal, and coronal), allowing a 2D distortion map to be obtained in all three planes as shown in Fig. 1 (top row). For 3D distortion characterization, a $465\times350\times168$ mm^3 phantom with over 4600 control points and 1.6 mm centroid-to-centroid spacing was used.

2.B. Image acquisition

MR images were acquired with a 1.0 Tesla (T) MR-SIM (Panorama High-Field Open Magnetic Resonance System, Philips Medical Systems, Cleveland, OH) using the integrated quadrature coil. The MR-SIM consists of a vertical magnetic field design with 45 cm anterior–posterior clearance of the physical aperture. To measure distortions resulting from GNL, the phantom was scanned with a 3D T1-weighted gradient echo (GE) sequence: TE/TR/flip angle of 5.54 ms/30 ms/28°, FOV $450\times450\times26$ mm^3, bandwidth 191 Hz/pixel, acquisition voxel dimensions $1\times1\times2$ mm^3, number of signal averages = 1, and acquisition duration of 5.6 min. Two scans were obtained in each of the three phantom orientations (the first with a positive read gradient polarity 4.48 mT/m and the second with a negative read gradient polarity −4.48 mT/m) so that the reverse gradient technique[14,16,19] could be used to isolate distortions due to GNL in all axes. During

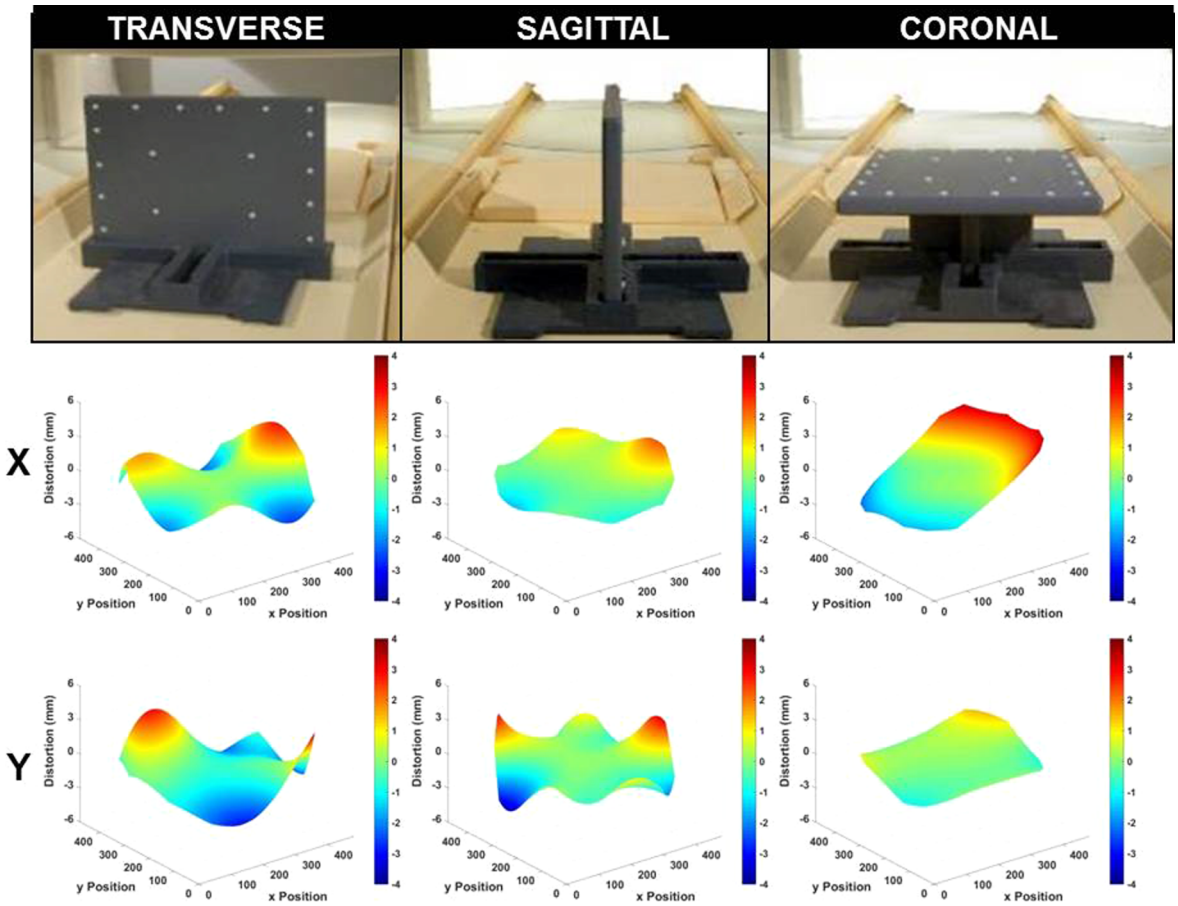

FIG. 1. (Top row) Setup of 2D distortion phantom. (Middle row) Corresponding x-axis distortion map (mm) vs image pixel location. (Bottom row) Corresponding y-axis distortion map (mm) vs image pixel location.

standard 3D GE imaging protocols, object dependent and B_0 distortions are only present in the frequency-encoding direction, while gradient distortions are present in all three directions. It is important to note that GNL is a property of the magnet and thus, independent of acquisition sequence. In this manner, the use of a 3D sequence with only one frequency encoding direction was necessary to isolate sequence-dependent distortions to a single axis. While a 3D spin echo (3DSE) sequence could have been used, a 3DSE acquisition would have substantially longer scan times than 3DGE and thus impede clinical efficiency. In addition, our selection of 3DGE is also consistent with the literature.[6,14,16] In the reverse gradient method, the same scan is repeated using opposite read gradient polarities. B_0 distortions will have opposite polarity when the polarity of the read gradient is reversed, while gradient distortions will remain constant. Therefore, the distortion due to GNL can be isolated by taking the average distortion of the two scans. A more detailed discussion of this method can be found in Baldwin *et al.*[16] Our scanner is equipped with vendor-supplied corrections to correct for gradient-related distortions that are derived from a spherical harmonic model. All scans were acquired with vendor-supplied 3D corrections enabled, which is consistent with our clinical practice.

For the 3D analysis, in order to sample the distortion in a larger superior-inferior (SI) direction, a batch file script was devised that communicated with the scanner to translate the 3D phantom in its axial orientation yielding a total scan extent of $465\times350\times400$ mm^3 (>13 800 landmarks). Two scans with reverse read gradient polarities were taken at each of the three locations within the bore so that the reverse gradient technique could be applied throughout the entire imaging volume.

It has been shown that eddy currents generated by rapidly pulsed gradients may potentially influence image distortion.[20] To verify that eddy currents do not adversely impact our distortion characterization, the phantom was scanned as above at four different TE settings (5.5, 13.8, 20.7, and 34.5 ms with TR = 50.9 ms) in three cardinal axes. TEs spanned a range similar to what has been reported in the literature[16] but modified *ad hoc* to yield acceptable image quality and resolve scanner conflicts. Using 5.5 ms as the baseline value, the mean shift in distortion measurements over all landmarks for each phantom orientation was calculated and plotted as a function of TE to identify possible trends.

2.C. Image analysis

To establish the position of each phantom control point (defined as the centroid), an automated program was developed in-house using MATLAB® (Mathworks, Natick, MA). First, images were generated by taking the maximum intensity projection of each of all 13 slices for each scan, which is consistent with our clinical protocol.[15] Control point detection was then conducted on each image with a combination of masking and thresholding, while a connectivity algorithm was used to further separate control points from increased noise at the field boundaries. The x and y positions (horizontal and vertical axes, respectively) were determined by finding the centroid of each control point and were compared to a binary template generated from the factory schematic of the phantom. Similar analysis was performed for the 3D phantom for all three axes. The total distortion of each control point was taken as the difference of the measured centroid positions from the known positions in the template. Once the distortions at each control point were determined, a full distortion map was interpolated by using singular value decomposition (SVD) to fit the data to a sixth-degree polynomial, which is similar to what has been reported in the literature.[21,22] Distortion maps were plotted and compared for each axis (week 1 shown in Fig. 1) and over the entire sampled FOV using the 3D phantom. Figure 3 illustrates a subset of distortion measurements plotted as a function of distance from isocenter.

2.D. Distortion correction

To correct for the distortion, the derived distortion map was used as a template to warp the distorted image and create a corrected image. However, since there is not necessarily a one-to-one correspondence between pixels in the distorted image and pixels in the corrected image, our algorithm steps through each pixel of the corrected image and determines the pixel's intensity from the distorted pixels that map to it (inverse warping). This ensures that no pixels in the corrected image are missed, and thus avoids "holes" in the corrected image. Because image distortion may cause compression and expansion of image volumes resulting in intensity changes that may not be fully resolved by pixel mapping, the corrected image was also multiplied by a Jacobian scaling factor as described in Doran *et al.*[6]

2.E. Temporal stability of distortion corrections

Temporal stability of large FOV distortion corrections and recommended measurement frequency are not currently known. Mah *et al.* measured distortion at four locations and showed temporal variations of less than 3 pixels over 18 months, although this was not characterized for large FOVs.[23] To characterize the stability of GNL distortion measurements, weekly scans of the 2D distortion phantom in all three axes were acquired over the course of six months (20 time points) using the reverse gradient technique. Differences from baseline (i.e., week 1) were assessed by generating difference maps and evaluating daily statistics.

3. RESULTS AND DISCUSSION

3.A. Distortion characterization at isocenter

Eddy currents were found to be appropriately compensated for with image distortion varying <0.2 mm over all TE settings (less than half of the pixel width and can be considered negligible). These results are in agreement with Baldwin *et al.* (<0.3 mm for a 3.0 T cylindrical magnet).[16] In 2000, Tanner *et al.* measured distortions of up to 1.3 mm with varying TE for their 1.5 T cylindrical bore magnet.[20] However, this

TABLE I. Week 1 gradient nonlinearity distortion statistics for three cardinal planes through isocenter where x and y refer to the horizontal and vertical axes of the respective planes. $P5$ and $P95$ describe the 5th and 95th percentiles of the distortion distribution, respectively.

Plane	Mean (mm)	StDev (mm)	$P5$ (mm)	$P95$ (mm)	Distortion > 1 mm (total % pixels)	Distortion > 2 mm (total % pixels)
Transverse (x)	0.07	1.10	−1.83	1.92	35	7
Transverse (y)	0.10	1.10	−1.5	2.15		
Sagittal (x)	0.03	0.64	−0.93	1.15	14	3
Sagittal (y)	−0.09	0.70	−1.23	1.11		
Coronal (x)	0.40	1.16	−1.32	2.50	40	14
Coronal (y)	0.04	0.40	−0.52	0.77		

early generation magnet had unshielded gradients; modern hardware and shielded gradients more readily compensate for eddy currents.

Figure 1 shows the maps of residual distortion resulting from GNL for the three cardinal planes at magnet isocenter, and Table I shows the corresponding distortion statistics across the entire 36×43 cm phantom. Although negligible near isocenter (less than the 1 mm pixel width), these distortions become greater than 1 mm as close as 9.5 cm from isocenter in the transverse plane, 12.5 cm in the sagittal plane, and 11.7 cm in the coronal plane. The largest distortion magnitudes occurred near the periphery of the usable FOV (~4 mm distortion at 20 cm from isocenter), where the usable FOV is defined by the furthest extent at which control points can be identified. These distortions are similar in magnitude to those measured without vendor corrections enabled for a 3 T magnet with cylindrical geometry by Baldwin *et al.*[16] GNL distortions for our vertical magnet were more pronounced in the left–right direction, particularly in the coronal plane as shown in the middle-right panel of Fig. 1. In the vertical magnet orientation, the maximum magnetic field gradient occurs in the right to left direction, which may contribute to the larger GNL distortion in this axis. It is also important to note that our measurements were non-negligible when 3D vendor distortion corrections were enabled, indicating that additional corrections are necessary for our magnet configuration.

Over six months, the coronal plane had the widest interquartile range, with 50% of the usable FOV having distortions between −0.5 and 1.25 mm, while the sagittal plane had the smallest, with 50% of the usable field of view having distortion between −0.25 and 0.25 mm. The transverse plane consistently has the largest distortions with maximum distortions of 4 mm, and a $P95$ of 2 mm. For any given daily distortion measurement over the six months, difference maps show 95% of voxels varied <0.6 mm from the baseline measurement (week 1) for all planes. This suggests that for routine QA, a higher frequency of GNL measurement is not necessary and these results support recent recommendations of annual measurement.[24]

3.B. 3D distortion characterization

As expected, distortion from GNL is much more pronounced in the peripheral voxels. Over the entire sampled volume, 65% of all voxels had non-negligible distortions (>1 mm), 26% of voxels distorted >2 mm, 9% > 3 mm, and 3% > 4 mm, with the largest distortion observed of ~7.4 mm at 23 cm radial distance from magnet isocenter. Figure 2 (Multimedia view) illustrates the 3D distortion results over the entire phantom volume before and after postprocessing corrections were applied. In the postcorrection dataset, nearly all measured distortions were reduced to less than 1 pixel width, with the exception of distant field corners up to a radial distance of 25 cm from magnet isocenter. This suggests that with appropriate postprocessing corrections, GNL distortions can be reduced to negligible levels despite substantial initial

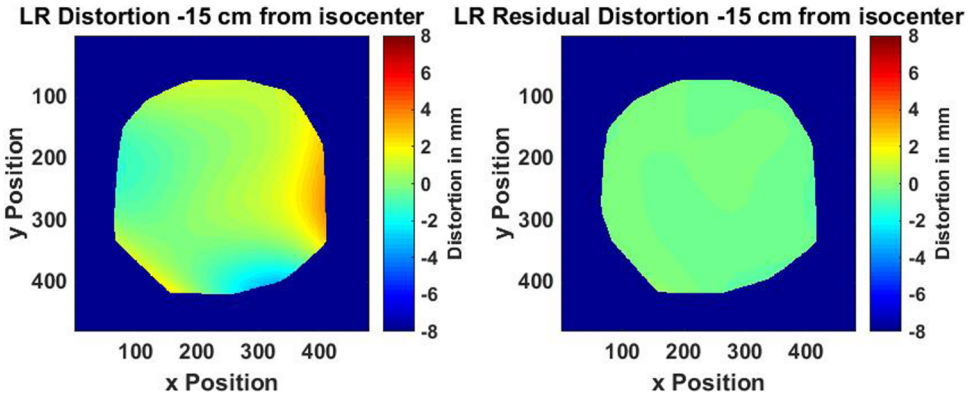

FIG. 2. Left–right (LR) distortion maps for the 3D phantom in the transverse plane. (Left) Quantified gradient nonlinearity distortion for the 3D phantom at 15 cm inferior of isocenter. (Right) Residual distortion after postprocessing corrections were applied. Results for the entire volume can be observed in Multimedia view. [URL: http://dx.doi.org/10.1118/1.4930245.1]

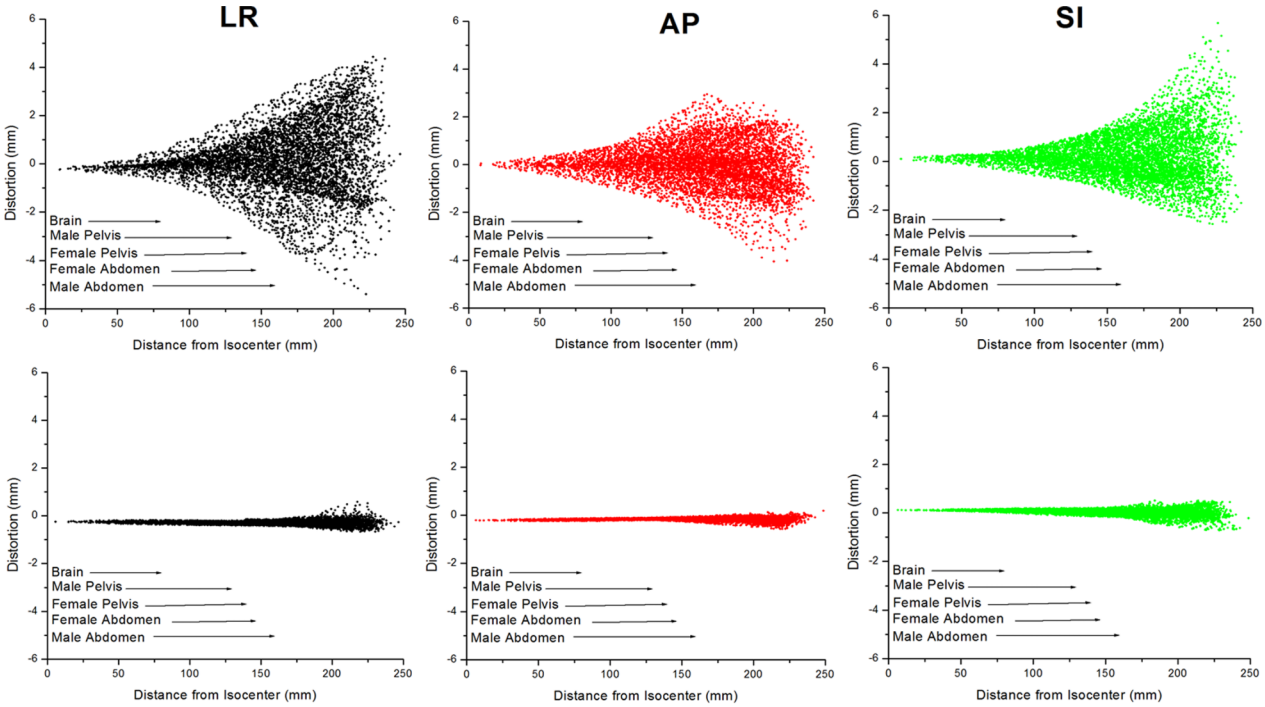

FIG. 3. (Top row) Distortion measurements (mm) as a function of distance from magnet isocenter (mm) for one scan. (Bottom row) Residual distortion after postprocessing corrections (mm) as a function of distance (mm). Arrows show the average radius of relevant anatomy of interest taken from the literature (Refs. 26–29 and 31).

GNL distortion for large FOVs. Similar results were reported by Doran *et al.*[6] and Baldwin *et al.*[16] with a possible cause of the remaining distortion being divergence of the polynomial fit at the boundaries.

Figure 3 shows the 3D stepped distortion map data plotted as a function of radial distance from magnet isocenter with the radii of typical anatomical structures also shown.[25–29] Initial vendor-supplied 3D distortion corrections maintained <1 mm distortion up to ~9.5 cm from isocenter although GNL became non-negligible as distance from isocenter increased. This suggests that to support MR-only RTP, additional corrections are necessary for anatomy >10 cm from isocenter for this magnet configuration. However, in another study by Wang *et al.*, it was suggested that shorter gradient coils could result in significantly higher GNL distortion.[17] This suggests that the GNL distortion measured for vertical magnet designs could be significantly worse than for the more commonly used cylindrical bore configuration.

Another solution to address GNL includes using a "step and shoot" technique where multiple couch longitudinal positions are used to segment large FOVs to facilitate imaging more of the anatomy of interest near isocenter.[24] Our open geometry allows for lateral table translation, thus lateral lesions such as breast cancer or sarcomas may be positioned at isocenter to further reduce the impact of GNL.

One limitation of this study is that it focused on GNL and did not address other sources of distortion such as those arising from field inhomogeneity, chemical shift, and magnetic susceptibility differences. Nevertheless, using higher readout bandwidths[14,24,30] and thoughtful sequence selection[31] have been shown to minimize these effects. A double echo gradient echo phase mapping method[14,32] can be used to measure and calculate sequence-dependent distortion maps which can then be used for corrections. Future work will include characterization of patient-dependent distortions for our magnet, including susceptibility, for relevant regions of interest.

4. CONCLUSION

Inherent distortions due to GNL were non-negligible for large FOVs with 3D vendor corrections enabled, thus necessitating a correction scheme to support MRI only treatment planning for anatomies >10 cm from isocenter. However, with postprocessing corrections, GNL was reduced to <1 mm for large FOVs. GNL measurements were stable over six months of clinical operation, thus supporting the application of correction maps in MR-only RTP.

ACKNOWLEDGMENTS

The authors would like to thank Mike Cavaliere, David Hearshen, and Weili Zheng for insightful discussions regarding GNL and eddy currents in MRI. Henry Ford Health System holds research agreements with Philips Healthcare. Research supported in part by NIH R01 Grant No. EB016079.

[a]Author to whom correspondence should be addressed. Electronic mail: churst2@hfhs.org

[1]M. Debois, R. Oyen, F. Maes, G. Verswijvel, G. Gatti, H. Bosmans, M. Feron, E. Bellon, G. Kutcher, H. Van Poppel, and L. Vanuytsel, "The contribution of magnetic resonance imaging to the three-dimensional treatment

planning of localized prostate cancer," Int. J. Radiat. Oncol., Biol., Phys. **45**, 857–865 (1999).
[2]R. C. Krempien, K. Schubert, D. Zierhut, M. C. Steckner, M. Treiber, W. Harms, U. Mende, D. Latz, M. Wannenmacher, and F. Wenz, "Open low-field magnetic resonance imaging in radiation therapy treatment planning," Int. J. Radiat. Oncol., Biol., Phys. **53**, 1350–1360 (2002).
[3]P. L. Roberson, P. W. McLaughlin, V. Narayana, S. Troyer, G. V. Hixson, and M. L. Kessler, "Use and uncertainties of mutual information for computed tomography/magnetic resonance (CT/MR) registration post permanent implant of the prostate," Med. Phys. **32**, 473–482 (2005).
[4]T. Nyholm, M. Nyberg, M. G. Karlsson, and M. Karlsson, "Systematisation of spatial uncertainties for comparison between a MR and a CT-based radiotherapy workflow for prostate treatments," Radiat. Oncol. **4**, 54 (2009).
[5]D. F. Dubois, W. S. Bice, Jr., and B. R. Prestige, "CT and MRI derived source localization error in a custom prostate phantom using automated image coregistration," Med. Phys. **28**, 2280–2284 (2001).
[6]S. J. Doran, L. Charles-Edwards, S. A. Reinsberg, and M. O. Leach, "A complete distortion correction for MR images: I. Gradient warp correction," Phys. Med. Biol. **50**, 1343–1361 (2005).
[7]D. Wang, D. M. Doddrell, and G. Cowin, "A novel phantom and method for comprehensive 3-dimensional measurement and correction of geometric distortion in magnetic resonance imaging," Magn. Reson. Imaging **22**, 529–542 (2004).
[8]J. Kim, C. Glide-Hurst, A. Doemer, N. Wen, B. Movsas, and I. J. Chetty, "Implementation of a novel algorithm for generating synthetic CT images from magnetic resonance imaging data sets for prostate cancer radiation therapy," Int. J. Radiat. Oncol., Biol., Phys. **91**, 39–47 (2015).
[9]S. H. Hsu, Y. Cao, K. Huang, M. Feng, and J. M. Balter, "Investigation of a method for generating synthetic CT models from MRI scans of the head and neck for radiation therapy," Phys. Med. Biol. **58**, 8419–8435 (2013).
[10]A. Johansson, M. Karlsson, and T. Nyholm, "CT substitute derived from MRI sequences with ultrashort echo time," Med. Phys. **38**, 2708–2714 (2011).
[11]T. Stanescu, H. S. Jans, N. Pervez, P. Stavrev, and B. G. Fallone, "A study on the magnetic resonance imaging (MRI)-based radiation treatment planning of intracranial lesions," Phys. Med. Biol. **53**, 3579–3593 (2008).
[12]B. H. Kristensen, F. J. Laursen, V. Logager, P. F. Geertsen, and A. Krarup-Hansen, "Dosimetric and geometric evaluation of an open low-field magnetic resonance simulator for radiotherapy treatment planning of brain tumours," Radiother. Oncol. **87**, 100–109 (2008).
[13]T. Stanescu, K. Wachowicz, and D. A. Jaffray, "Characterization of tissue magnetic susceptibility-induced distortions for MRIgRT," Med. Phys. **39**, 7185–7193 (2012).
[14]L. N. Baldwin, K. Wachowicz, and B. G. Fallone, "A two-step scheme for distortion rectification of magnetic resonance images," Med. Phys. **36**, 3917–3926 (2009).
[15]C. K. Glide-Hurst, N. Wen, D. Hearshen, J. Kim, M. Pantelic, B. Zhao, T. Mancell, K. Levin, B. Movsas, I. J. Chetty, and M. S. Siddiqui, "Initial clinical experience with a radiation oncology dedicated open 1.0 T MR-simulation," J. Appl. Clin. Med. Phys. **16**, 218–240 (2015).
[16]L. N. Baldwin, K. Wachowicz, S. D. Thomas, R. Rivest, and B. G. Fallone, "Characterization, prediction, and correction of geometric distortion in 3 T MR images," Med. Phys. **34**, 388–399 (2007).
[17]D. Wang, W. Strugnell, G. Cowin, D. M. Doddrell, and R. Slaughter, "Geometric distortion in clinical MRI systems Part I: Evaluation using a 3D phantom," Magn. Reson. Imaging **22**, 1211–1221 (2004).
[18]C. J. Bakker, M. A. Moerland, R. Bhagwandien, and R. Beersma, "Analysis of machine-dependent and object-induced geometric distortion in 2DFT MR imaging," Magn. Reson. Imaging **10**, 597–608 (1992).
[19]H. Chang and J. M. Fitzpatrick, "A technique for accurate magnetic resonance imaging in the presence of field inhomogeneities," IEEE Trans. Med. Imaging **11**, 319–329 (1992).
[20]S. F. Tanner, D. J. Finnigan, V. S. Khoo, P. Mayles, D. P. Dearnaley, and M. O. Leach, "Radiotherapy planning of the pelvis using distortion corrected MR images: The removal of system distortions," Phys. Med. Biol. **45**, 2117–2132 (2000).
[21]C. Hong, D. H. Lee, and B. S. Han, "Characteristics of geometric distortion correction with increasing field-of-view in open-configuration MRI," Magn. Reson. Imaging **32**, 786–790 (2014).
[22]D. Wang and Z. Yang, "A detailed study on the use of polynomial functions for modeling geometric distortion in magnetic resonance imaging," Med. Phys. **35**, 908–916 (2008).
[23]D. Mah, M. Steckner, E. Palacio, R. Mitra, T. Richardson, and G. E. Hanks, "Characteristics and quality assurance of a dedicated open 0.23 T MRI for radiation therapy simulation," Med. Phys. **29**, 2541–2547 (2002).
[24]E. S. Paulson, B. Erickson, C. Schultz, and X. Allen Li, "Comprehensive MRI simulation methodology using a dedicated MRI scanner in radiation oncology for external beam radiation treatment planning," Med. Phys. **42**, 28–39 (2015).
[25]C. D. Fryar, Q. Gu, and C. L. Ogden (2012): Anthropometric reference data for children and adults: United States, 2007–2010. Vital Health Stat11 (252), available at: http://www.cdc.gov/nchs/data/series/sr_11/sr11_252.pdf. Accessed September, 2015.
[26]H. Gray and W. H. Lewis, *Anatomy of the Human Body*, 20th ed. (Lea & Febiger, Philadelphia, New York, 1918).
[27]A. Walker, G. Liney, P. Metcalfe, and L. Holloway, "MRI distortion: Considerations for MRI based radiotherapy treatment planning," Australas. Phys. Eng. Sci. Med. **37**, 103–113 (2014).
[28]W. Platzer, *Color Atlas of Human Anatomy. Volume 1 Locomotor System, 6th revised and enlarged edition* (Thieme, Stuttgart, New York, 2009).
[29]A. H. Buck and T. L. Stedman, *A Reference Handbook of the Medical Sciences Embracing the Entire Range of Scientific and Practical Medicine and Allied Science, new edition* (W. Wood and Company, New York, NY, 1900).
[30]A. Fransson, P. Andreo, and R. Potter, "Aspects of MR image distortions in radiotherapy treatment planning," Strahlenther. Onkol. **177**, 59–73 (2001).
[31]K. Wachowicz, T. Stanescu, S. D. Thomas, and B. G. Fallone, "Implications of tissue magnetic susceptibility-related distortion on the rotating magnet in an MR-linac design," Med. Phys. **37**, 1714–1721 (2010).
[32]P. Jezzard and R. S. Balaban, "Correction for geometric distortion in echo planar images from B0 field variations," Magn. Reson. Med. **34**, 65–73 (1995).